PAPER

Check for updates

SiC$_x$N$_y$:Fe films as a tunable ferromagnetic material with tailored conductivity†

Roman Pushkarev, ID *[a] Nadezhda Fainer,[a] Victor Kirienko,[b] Alexey Matsynin,[c] Vladimir Nadolinnyy,[a] Ivan Merenkov, ID [ad] Svetlana Trubina,[a] Simon Ehrenburg[ae] and Kristina Kvashnina[fg]

Amorphous ferromagnetic materials with variable composition are promising candidates for application in rapidly-growing technological fields, such as spintronics. However, the significant downside of current state-of-the-art materials is a conductivity mismatch between the injector and the semiconductor, which often is associated with the inability to control and precisely tailor the magnetic properties and conductivity. We report on the synthesis of soft-magnetic SiC$_x$N$_y$:Fe films with a saturation magnetization of 20 emu cm^{-3} and a conductivity similar to the one of Si, which is crucial for possible applications. XRD with synchrotron radiation and EXAFS revealed the complex composite structure of the films: crystals of Fe$_3$Si, Fe$_5$Si$_3$, SiC and graphite are embedded into the amorphous matrix of SiC$_x$N$_y$. Variation of the deposition conditions allowed us to separately control the magnetic properties through the iron concentration and the conductivity of the material through the amorphous SiC$_x$N$_y$ matrix composition. The reported results revealed significant potential of SiC$_x$N$_y$:Fe films as a prospective object for analysis of spin-polarized transport in amorphous semiconductors and for application in the field of spintronics.

Introduction

The development of new technology fields requires new materials with a wide variety of functional properties. Multi-functional materials are designed in such a way that one can tailor their properties by changing the composition, temperature, electro-magnetic field, *etc.* An exciting example of properties to combine is ferromagnetism and semiconductivity. Tunable charge transfer properties combined with ferromagnetic ordering may solve existing problems in semiconductor spintronics and magnetic sensor materials. Different approaches were used in order to obtain materials possessing the desired combination. One of the most widely investigated examples of magnetic semiconductors is ZnO or A^{III}B^V doped with atoms of d-elements.[1–6] Despite the fact of achieving ferromagnetic ordering in these materials, several problems, such as a low Curie temperature (lower than room temperature) and limited solubility of metals in the semiconducting matrix, remain unsolved.[7–9] Control over ferro-magnetic material conductivity is another essential task for spintronics. The contact resistance of a spin injector needs to be engineered at the optimum level, otherwise, the conductivity mismatch will result in the absence of spin-polarized current.[10,11]

Ferromagnetic semiconductors with an amorphous matrix are considered as a possible solution for these problems.[12] These materials possess properties exceeding the ones of their crystal analogs. A subclass of ferromagnetic semiconductors with an amorphous matrix is granular systems, where magnetic particles are embedded into an amorphous matrix of an insulator. The magnetic metal particles combined with the insulator matrix give rise to the formation of a semiconducting composite with magnetic ordering.[13,14] Unfortunately, the goal to control the conductivity and magnetic properties of these composites in a precise way remains unreached. A possible solution to this obstacle is the application of an amorphous matrix with variable composition, such as SiC$_x$N$_y$, instead of ones with fixed stoichiometry. One can tune the conductivity of SiC$_x$N$_y$ in a very wide range.[15,16] Through the variation of the matrix conductivity, one can control the conductivity of the composite material where magnetic iron-containing particles

a Nikolaev Institute of Inorganic Chemistry, Siberian Branch of Russian Academy of Sciences, pr. Acad. Lavrent'ev, 3, Novosibirsk, 630090, Russia. E-mail: pushkarev@niic.nsc.ru

b Rzhanov Institute of Semiconductor Physics, Siberian Branch of Russian Academy of Sciences, pr. Acad. Lavrent'ev, 13, Novosibirsk, 630090, Russia

c Kirensky Institute of Physics, Siberian Branch of Russian Academy of Sciences, Akademgorodok 50, 38, Krasnoyarsk, 660036, Russia

d Ural Federal University, Ekaterinburg, st. Mira, 19, 620002, Russia

e Budker Institute of Nuclear Physics, Siberian Branch Russian Academy of Sciences, pr. Acad. Lavrent'ev, 11, Novosibirsk, 630090, Russia

f Rossendorf Beamline at ESRF, 38043, Grenoble, France

g HZDR, Institute of Resource Ecology, 01314, Dresden, Germany

† Electronic supplementary information (ESI) available. See DOI: 10.1039/c9tc00299e

are embedded into the SiC_xN_y matrix. It will allow one to create ferromagnetic semiconductors or insulators, which are useful either for injection or detection of spin-polarized current.[17,18] Tunable conductivity of a ferromagnetic material is a useful tool for overcoming the conductivity mismatch problem.[19]

Earlier reports devoted to the creation of magnetic materials based on SiC_xN_y were focused on ceramics,[5] while films and other low-dimensional materials are required for building of spintronics devices. Also, no information about the conductance of these composites, which is essential for spintronics, was provided.

It is worth noting that study of the conductivity mechanism and the origin of ferromagnetism in these materials is of the essence for potential application in spintronics. Considerable advances in the study of these mechanisms were achieved for materials with ordered crystal structure, such as diluted magnetic semiconductors based on ZnO and $A^{III}B^V$ compounds.[20,21] Still, this work is on-going and requires more efforts before the origin of room temperature ferromagnetism will be established.[22] The conductivity and ferromagnetism mechanisms are significantly less studied for materials with an amorphous structure. This work provides new insight into the electron transport and magnetic properties of complex materials with an amorphous structure. The presented results may become a basis for more detailed study of spin-polarized transport mechanisms in amorphous semiconductors useful for spintronics technology.

Experimental part

Deposition procedure

The SiC_xN_y:Fe films were synthesized using a chemical vapor deposition technique by the thermal decomposition of three different gaseous mixtures. Tris(diethylamino)silane (TDEAS) and ferrocene were used as sources of Si, C, N, and Fe, respectively, and were common for all the mixtures. In order to tailor the composition of the films in a precise way, we used either helium, or hydrogen, or ammonia as the third component of the gas mixture. The first one is an inert gas, while the other two may change the composition of the deposited films, e.g. in the SiC_xN_y synthesis procedures introduction of ammonia results in the nitrogen concentration rising.[23,24]

The deposition procedure was carried out in a horizontal quartz tube. The deposition conditions are described as follows: a deposition temperature range of 800–1000 °C, and partial pressures of the components $P_{TDEAS} = 5 \times 10^{-2}$ Torr, $P_{Ferrocene} = 3 \times 10^{-2}$ Torr and $P_{gas} = 3 \times 10^{-2}$ Torr. The residual pressure was about $(7–8) \times 10^{-4}$ Torr. Preliminary degreasing followed by chemical treatment in HF of the Si(100) wafers was performed for all the specimens obtained.

Characterization methods

The microstructure of the surface of the film was studied using a scanning electron JSM-6700F microscope with a resolution of 1 nm, and the elemental composition was examined by energy dispersive spectroscopy (EDS) with an EX-23000VU detector for this microscope. All the IR absorption spectra of the films were recorded on an FTIR SCIMITAR FTS 2000 spectrometer in the range 300–4000 cm^{-1}. The FTIR spectra were normalized to the film thickness and fitted with Gaussian profile functions using Origin software. The Raman spectra were recorded using a Triplemate, Spex spectrometer equipped with an argon ion laser with a wavelength of 488 nm. The phase composition of the films was studied on the "Precision diffractometry and anomalous scattering" station of the "Siberian Synchrotron and Terahertz Radiation Centre" (Novosibirsk, Russia) using the Bragg–Brentano experimental geometry. The incident beam wavelength was set at 1.5410 Å.

The EXAFS (extended X-ray absorption fine structure) spectra of the SiC_xN_y:Fe films were measured at the BM20 beamline channel, ESRF, Grenoble, France. Plates with films were glued to a table and placed under a monochromatic synchrotron radiation beam at an angle of about 3°. The spectra were measured at the FeK absorption edge in the energy range 6867–8091 eV, which corresponds to the wave-number k range up to 16 Å^{-1} (the X-ray FeK absorption edge is 7112 eV). The spectra were measured under fluorescence conditions with a 12-channel Ge detector. Si(111) was used as a crystal-monochromator. Two mirrors with Rh coatings were used to focus the beam in the horizontal and vertical planes. The quantum flux for recording spectra was approximately 7×10^{10} photons per s in a beam 200 μm × 5 mm in size. The local surroundings modelling was carried out using EXCURVE 98.

EPR spectra were recorded on a modified Varian E-109 spectrometer at 9.5 GHz and a Bruker ELEXSYS 500 at 9.44 GHz. 2,2-Diphenyl-1-picrylhydrazyl (DPPH) and Mn^{2+} were used as g-factor standards, respectively.

The magnetic properties of the films were investigated with a torque magnetometer. The procedure of the measurements is described elsewhere.[25] The equation

$$\Psi H/L = 1/M_s V + H/K_\perp V,$$

where L is the torque moment, H – external magnetic field, M_s – saturation magnetization, V – specimen volume, $K_\perp$ – perpendicular anisotropy constant, is suitable in the case when the direction of the magnetic field applied to the specimen forms a small angle Ψ with the specimen plane. Studying $\Psi H/L$ as a function of H allows one to determine M_s and $K_\perp$. All measurements were carried out at room temperature in the magnetic field range of 0–2000 Oe.

The I–V curve analysis of the Al/SiC_xN_y:Fe/Si structures allowed us to determine the conductivity of the SiC_xN_y:Fe films at room temperature. In order to create such a multilayer structure Al was deposited as an electrode on the surface of SiC_xN_y:Fe/Si(100). The surface of the Al electrode was 0.7×0.7 mm^2. Since the thickness of the films may vary due to the different deposition rates at various temperatures, the electric conductivity was determined at an electric field of 10^5 V cm^{-1}.

This journal is © The Royal Society of Chemistry 2019

J. Mater. Chem. C, 2019, **7**, 4250–4258 | 4251

Results and discussion

Structure and morphology of SiC_xN_y:Fe films

As mentioned earlier, control over the functional properties of SiC_xN_y:Fe films is possible through the variation of the structure and elemental composition. By changing the deposition temperature and gas phase composition we were able to synthesize films with different elemental composition as depicted in Fig. 1. In the case of deposition from gaseous mixtures containing helium or hydrogen, the dominance of carbon in the film composition is obvious. The elemental composition of the films obtained from the helium-containing mixture changes with the deposition temperature growing: the carbon concentration grows from 45 at% to 60 at%, while the silicon concentration becomes lower from 38 at% to 20 at% (Fig. 1). The nitrogen concentration remains approximately constant ∼15 at%. Deposition from a mixture of ferrocene, TDEAS, and hydrogen leads to the same tendencies for the elemental composition *vs.* deposition temperatures. It is worth mentioning that such dominance of carbon in the film composition may originate from the presence of a free carbon phase.[26] The composition of the films deposited from the ammonia-containing mixture differs significantly from the composition of the films mentioned earlier. The main element, in this case, is silicon with a concentration of 40–45 at%. The nitrogen concentration is about 25–30 at%, which is significantly higher than for the films deposited from the helium or hydrogen-containing mixtures. Fe concentration growth with the deposition temperature rising is the general tendency for all gaseous mixtures. Films deposited at 800 °C contain ∼2–3 at% of iron. Higher deposition temperatures allow one to obtain films containing up to 10 at% of iron. The variation of the Fe concentration provides an opportunity to control the magnetic properties of the films. Oxygen is present in the films as an admixture with a concentration of 0–2 at%.

Previous studies of amorphous SiC_xN_y indicated that this substance can be described as tetrahedral coordination of C and N atoms to Si atoms. Thus, structural fragments of Si–C–Si, Si–N–Si, and Si–C–C–Si are the main building blocks of
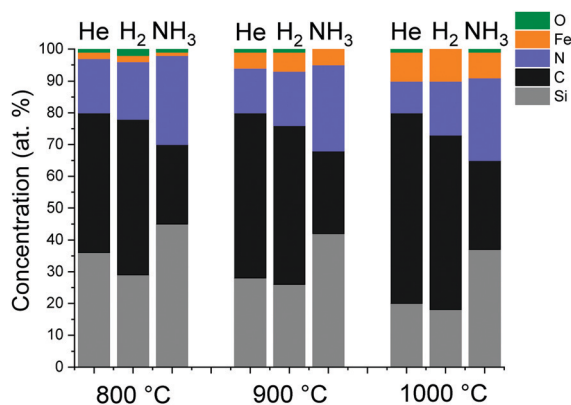

Fig. 1 Elemental composition of SiC_xN_y:Fe films deposited at different temperatures (denoted at the bottom) from gaseous mixtures containing He, H_2 or NH_3.
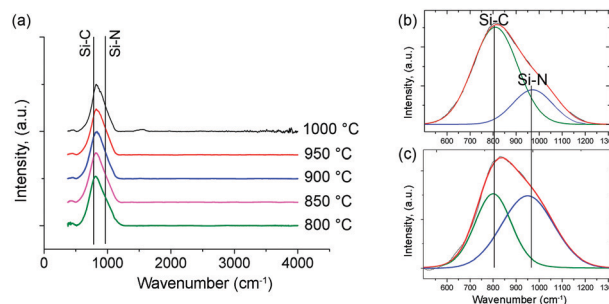

Fig. 2 (a) FTIR spectra of SiC_xN_y:Fe films deposited from a gaseous mixture of TDEAS, ferrocene, and helium at different temperatures, and (b and c) FTIR spectra (in the range of 500–1300 cm^{-1}) of SiC_xN_y:Fe films deposited from hydrogen and ammonia-containing gas mixtures, respectively.

amorphous SiC_xN_y.[27–29] According to this structure model, C–N bonds are absent in this material. Therefore, we assume that the structure of the amorphous matrix of SiC_xN_y:Fe films is similar to the one of SiC_xN_y films. This suggestion was confirmed by the FTIR spectral analysis of SiC_xN_y:Fe films (Fig. 2).

The common feature of the FTIR spectra of the SiC_xN_y:Fe films deposited in this work is an asymmetric peak with a maximum at 850 cm^{-1}. This broad peak consists of two components related to the vibration of Si–C and Si–N bonds centered at 800 and 950 cm^{-1}, respectively (Fig. 2a). As one can see, peaks of C–N related fragments are absent. We concluded that the amorphous part of the material has a structure similar to the one of SiC_xN_y described earlier: Si atoms with C and N tetrahedral coordination.

In order to compare the FTIR spectra of the films deposited under different experimental conditions (*e.g.*, deposition temperature, and gaseous mixture composition) their intensity was divided by the film thickness. Since the broad peak intensity does not depend on the deposition temperature, we concluded that the composition of the SiC_xN_y matrix does not depend on the deposition temperature. Therefore, it can be concluded that a rising concentration of carbon with a growing deposition temperature promotes the formation of a free carbon phase. The small peak around 1500 cm^{-1} emerging in the case of deposition at 1000 °C can be attributed to the disordered graphite phase. The appearance of this peak is in agreement with the above-mentioned conclusion. Due to the limitations of the FTIR method for analysis of carbon-containing phases, Raman spectroscopy is required to study the formation of disordered graphite in more detail. The most interesting tendency in the FTIR spectra is observed for the intensity ratio $I_{Si–C}/I_{Si–N}$. This ratio changes with the gas mixture composition being varied. The deposition from a gas mixture of ferrocene, TDEAS and helium results in $I_{Si–C}/I_{Si–N}$ = 2.4–2.5. Such Si–C bond dominance in the FTIR spectra of SiC_xN_y films synthesized by the CVD technique at temperatures higher than 400 °C was mentioned earlier by Wrobel.[30–32] While the substitution of helium for hydrogen does not affect the intensity ratio (Fig. 2b), deposition from the ammonia-containing mixture results in the formation of films with the Si–N bond vibration peak having a

4252 | *J. Mater. Chem. C*, 2019, **7**, 4250–4258

This journal is © The Royal Society of Chemistry 2019

similar intensity to the one of the Si–C peak (Fig. 2c). The ratio of I_{Si-C}/I_{Si-N}, in this case, is significantly lower (0.7–0.8). This change indicates that the structure of the amorphous SiC_xN_y matrix changes from the one close to amorphous SiC_x to the one enriched with Si–N bonds similar to amorphous SiN_x. We assume that control over the amorphous matrix composition will provide us with an opportunity to change the functional properties of the material (e.g. relative conductivity).

As mentioned, in the case of helium and hydrogen-containing mixtures carbon is the main element of the films. The excessive C concentration leads to the formation of free carbon phases such as amorphous carbon and graphite, which was confirmed by Raman spectroscopy. The Raman spectra of SiC_xN_y:Fe films (Fig. 3a) contain two main peaks: D and G modes related to the different states of the carbon phase.[33] The relative intensity and position of the D and G modes provide valuable information about the structure of carbon species. In the case of the films deposited from the helium-containing mixture in the temperature range of 800–900 °C the D mode is centered at $\sim$1360 cm^{-1}, while the G mode center is positioned at 1520 cm^{-1} (Fig. 3b). The position of the peaks combined with the relative intensity of I_D/I_G = 1–1.5 allows us to conclude that the majority of free carbon exists in an amorphous form. Deposition at higher temperatures results in a shift of the G mode center to higher wavenumber (1580 cm^{-1}), which is evidence of carbon graphitization (Fig. 3c). This tendency for graphitization at elevated temperatures is well known and may influence the electrical conductivity of the films. The Raman spectra of SiC_xN_y:Fe films deposited from hydrogen-containing mixtures also have the same D and G modes, but the shift of the latter one to higher wavenumbers occurs at a higher temperature of 1000 °C. Thus, the hydrogen slightly influences the carbon phase composition and has almost no effect on the SiC_xN_y matrix. In the case of deposition using the ammonia-containing gas mixture the Raman spectra are less intense, which indicates a lower carbon concentration. In addition, the G mode center shifts to higher wavenumbers at the same deposition temperature as in the case of the hydrogen-containing mixture. Thus, the variation of the gas mixture composition by changing helium for hydrogen or ammonia provides us with an opportunity to control the free carbon phase composition in the SiC_xN_y:Fe films.

The morphology of 2D materials, such as films, is a crucial parameter which may have a great influence on their functional properties. The surface of the films deposited from the 3 gaseous mixtures changes similarly with the deposition temperature growing. The morphology of the films deposited in the temperature range of 800–1000 °C with ΔT = 50 °C from the helium-containing mixture is depicted in Fig. 4. Deposition at 800 °C leads to the formation of a surface similar to the one of the amorphous SiC_xN_y films. At this temperature, the rate of ferrocene decomposition is low compared to the decomposition rate (DR) of TDEAS. As mentioned earlier, the concentration of iron does not exceed 3 at%. Elevation of the deposition temperature up to 850 °C and higher promotes the ferrocene decomposition with a rate sufficient to reach an iron atom concentration in the film up to 10 at%. The morphology of the films obtained at 900 °C has a globule-like structure. As one can see, the surface of the films deposited at 850 °C is composed of nuclei of the globules, which precedes the formation of the morphology of the films synthesized at 900 °C. Further deposition temperature elevation results in a higher iron concentration and formation of small grains on the film surface with a size of 50–70 nm, while the size of globules obtained in the case of deposition at 900 °C varies in the range of 0.5–4 μm.

Formation of globe-like structures can be described with a model of a "core–shell" structure, where the core is the nucleus of the crystal phase and the shell is represented by an amorphous substance. It was shown in our previous work[34] that the formation of crystallites inside the amorphous matrix begins at temperatures around 900 °C, making the scenario of "core–shell" structure formation possible. Similar results were earlier mentioned for different carbides, nitrides, and carbon materials.[35–41] At higher deposition temperatures, the DR of ferrocene is much higher, resulting in the formation of a large number of crystal nuclei. Therefore, the surface of films deposited above 900 °C has a granular-like structure.

In order to study the structure of the films in more detail, we used XRD with a synchrotron radiation source. Conventional X-ray diffractometers do not provide sufficient beam brightness,
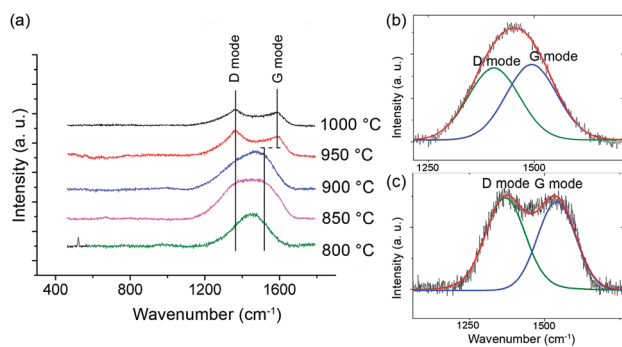

Fig. 3 (a) Raman spectra of SiC_xN_y:Fe films deposited from a gaseous mixture of TDEAS, ferrocene, and helium, and (b and c) detailed Raman spectra of the films deposited at 800 °C and 1000 °C, respectively.
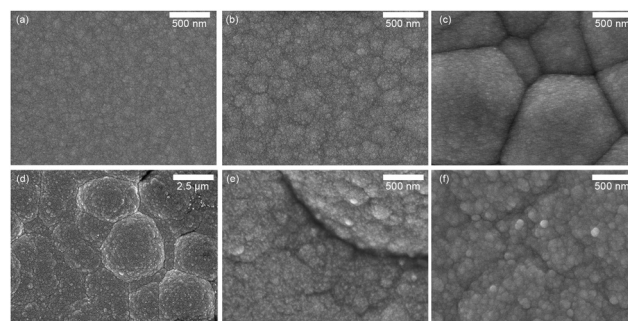

Fig. 4 Surface morphology of SiC_xN_y:Fe films deposited from a gaseous mixture of TDEAS, ferrocene, and helium at (a) 800 °C, (b) 850 °C, (c) 900 °C, (d and e) 950 °C, and (f) 1000 °C.
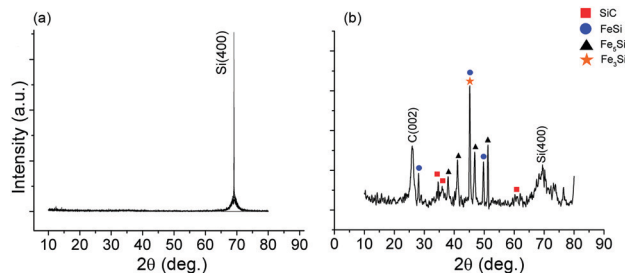
Fig. 5 XRD patterns of SiC_xN_y:Fe films deposited from a gaseous mixture of TDEAS, ferrocene, and helium at (a) 800 °C, and (b) 1000 °C.

making it difficult to analyze the composition of composite films with small crystallites. The SiC_xN_y:Fe films deposited at temperatures lower than 900 °C have an amorphous structure with no significant amount of crystallite inclusions (Fig. 5a). At higher deposition temperatures formation of Fe_5Si_3, Fe_3Si, FeSi, β-SiC, and graphite crystallites occurs (Fig. 5b). Unfortunately, it is difficult to conduct qualitative analysis due to the fact that the major peak at 45° can be attributed to both FeSi and Fe_5Si_3 phases. Therefore, additional structure analysis is required.

It is worth mentioning that the deposition of SiC_xN_y under the same conditions without the introduction of ferrocene leads to the formation of amorphous films without any crystallites embedded into an amorphous matrix.[42] Therefore, we concluded that the formation of iron-containing species serves as a driving force for the silicon carbide and carbon crystallization. This phenomenon could be described with the formation of a Fe–Si–C solid solution, which promotes the crystallization of crystallites composed of light elements, such as Si and C.[43]

The non-equilibrium nature of the CVD process and the local equilibrium is the reason why the mixture of silicides is formed. The phase diagram of the Fe–Si system has a field of Fe_3Si and Fe_5Si_3 coexistence in the temperature region of 800–1000 °C. Moreover, there is a field of Fe_5Si_3 and FeSi coexistence in the same temperature region with slightly higher silicon concentration. The existence of this phase field might be the reason for the formation of different iron silicides. Also, such a variety of silicides is possible due to their interconversion, described earlier.[44]

Due to the presence of multiple iron-containing phases, it is necessary to conduct additional analysis in order to establish which phase is dominant. EXAFS was used as a tool for analysis of the films deposited from the helium- and ammonia-containing gas mixtures. The moduli of Fourier transform magnitudes $|F(R)|$ for the experimental FeK EXAFS spectra of the SiC_xN_y:Fe films are presented in Fig. 6. One can see that the spectrum of the film deposited from the He-containing mixture differs significantly from the one deposited from the NH_3-containing mixture. The higher intensities in the case of the former one reveal its better crystallinity. According to the XRD of the sample deposited from the He-containing mixture it contains FeSi, Fe_3Si, and Fe_5Si_3 in unknown concentrations. The analysis of the local environment of the iron atoms in this
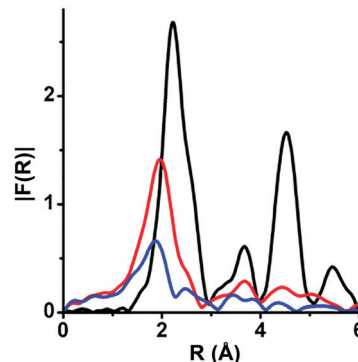

Fig. 6 Moduli of Fourier transform magnitudes $|F(R)|$ for experimental FeK EXAFS spectra of SiC_xN_y:Fe films deposited from a gaseous mixture of TDEAS, ferrocene, and helium at 1000 °C (red line), or NH_3 at 1000 °C (blue line), and the reference Fe foil (black line).

film pointed out the dominance of the Fe_3Si phase (interatomic distances in the 1st coordination sphere R(Fe–Fe) = 2.48 Å; R(Fe–Si) = 2.83 Å) with the concentration ∼60%, while FeSi (interatomic distances in the 1st coordination sphere R(Fe–Fe) = 2.76 Å; R(Fe–Si) = 2.35 Å) has a concentration of ∼30%. These results allow us to conclude that Fe_5Si_3 has a rather low concentration or is even absent in this case. The analysis of the film deposited from the NH_3-containing mixture revealed the dominant concentration of the Fe_5Si_3 phase with interatomic distances of R(Fe–Si) = 2.35 Å; R(Fe–Fe) = 2.36 Å; and R(Fe–Fe) = 2.85 Å. The presence of Fe_3Si and Fe_5Si_3 crystals explains the ferromagnetic properties of the SiC_xN_y films, but the reason behind the crystal composition changing yet remains unclear. A possible explanation for the coexistence of different silicides was given earlier, but their interconversion is a question for further study. The answer to this question may provide an efficient tool to control the phase composition of iron silicides and, therefore, the magnetic properties of SiC_xN_y:Fe films in a very precise way.

EPR was used to carry out a general analysis of magnetic ordering in the SiC_xN_y:Fe films. The EPR spectrum of the film deposited at 850 °C from the helium-containing mixture has one broad peak with a g-factor of 2.056 (Fig. 7). This value

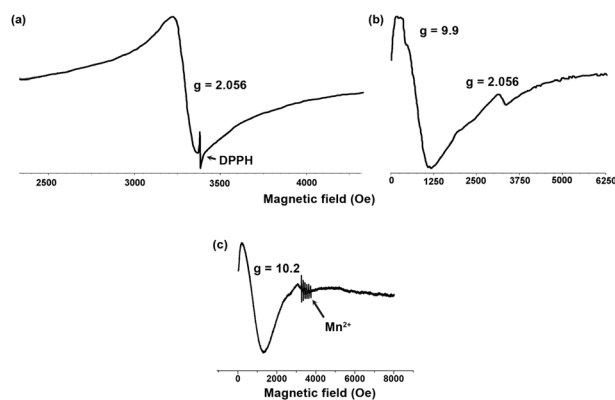**Fig. 7** EPR spectra of SiC_xN_y:Fe films deposited from a gaseous mixture of TDEAS, ferrocene, and helium at (a) 800 °C, (b) 900 °C, and (c) 1000 °C.

4254 | *J. Mater. Chem. C*, 2019, **7**, 4250–4258

This journal is © The Royal Society of Chemistry 2019

indicates the existence of paramagnetic centers with an electron spin $s = 1/2$. According to earlier research,[45] this signal may be assigned to Fe^{3+} embedded into the amorphous matrix of silicon carbonitride. According to the EDS analysis, the iron concentration in films deposited in the temperature interval of 800–900 °C is about 2–3 at%. In these conditions formation of iron-containing crystallites is unfavorable, thus, iron exists as Fe^{3+} ions distributed in the amorphous SiC_xN_y matrix. The absence of crystal phases of any kind which may possess paramagnetic properties was confirmed by XRD with synchrotron radiation. Also, it is worth noting that the undoped SiC_xN_y films deposited from the mixture of TDEAS and helium also possess paramagnetic resonance with significantly lower intensity. It may be due to the formation of dangling bonds in the amorphous matrix or the existence of small crystals (< 5 nm) of defective graphite.[46] Still, the iron-doped films have an EPR signal with higher intensity when the iron concentration is about 2–3 at%. Qualitative analysis of the EPR spectrum of the film deposited at 900 °C indicated the ferromagnetic nature of the specimen. The signal with $g = 9.9$ relates to ferromagnetic resonance which originates from iron-containing phases. The formation of FeSi crystallites starts in these conditions. According to the phase diagram of the Fe–Si binary system[43] at temperatures close to 900 °C FeSi may coexist with Fe_5Si_3, which is ferromagnetic.[47] Moreover, FeSi itself may possess ferromagnetic properties while existing in the nanocrystallite state.[48,49] The signal with $g \sim 2$ is still present, but its intensity is lower than the one of the signal described above. When the deposition temperature is elevated to 1000 °C, the intensity of the signal with $g \sim 2$ becomes negligible compared to the signal with $g = 9.9$. The formation of ferromagnetic phases, in this case, was confirmed by XRD and EXAFS analysis. Similar tendencies were observed for gaseous mixtures containing hydrogen or ammonia.

Functional properties of the SiC_xN_y:Fe films

More detailed analysis of magnetic properties was carried out using the vibration magnetometer technique. Fig. 8 shows the magnetization vs. magnetic field dependencies for the SiC_xN_y:Fe films deposited in the temperature range of 900–1000 °C. The saturation magnetization for the ferromagnetic films deposited

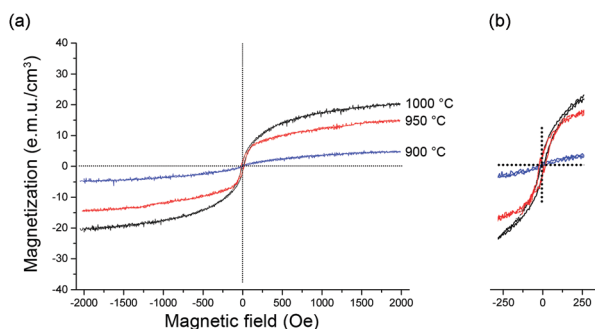**Table 1** Conductivity and saturation magnetization of SiC_xN_y:Fe films deposited in the temperature range of 800–1000 °C

Additional gas	Deposition temperature, °C	Conductivity, S cm^{-1}	Saturation magnetization, emu cm^{-3}
He	800	4.3×10^{-5}	
	900	3.6×10^{-4}	5 ± 1
	1000	6.9×10^{-4}	20 ± 2
H_2	800	1.6×10^{-6}	
	900	3.6×10^{-6}	5 ± 1
	1000	2.0×10^{-4}	18 ± 2
NH_3	800	10^{-12}	
	900	1.6×10^{-7}	5 ± 1
	1000	2.0×10^{-5}	20 ± 2

at temperatures of 900 °C and higher grows with the deposition temperature rising. The films deposited at temperatures lower than 900 °C do not possess ferromagnetic properties due to the low iron concentration and absence of ferromagnetic phases. A low iron concentration results in low magnetization values below the detection threshold. The coercivity of the ferromagnetic films deposited above 900 °C does not exceed 20 Oe, making these films soft-magnetic materials. The value of 20 Oe is in agreement with the previously reported coercivity for nanosized Fe_5Si_3 and Fe_3Si phases.[47] The Curie temperature of the sample containing Fe_5Si_3 is close to 400 K, which is higher than room temperature,[50] which makes this material promising for spintronics applications. Table 1 summarizes the saturation magnetization of the SiC_xN_y:Fe films synthesized under different conditions. One can see that the tendencies of the magnetization change are general for all gas mixtures: the magnetization grows with the deposition temperature rising.

Thus, it can be concluded that iron silicide phases formed in the composite material are the main reason for the ferromagnetic properties of the films. Despite the fact of different iron atom distributions between iron silicides in the case of deposition from He- and NH_3-containing mixtures the magnetic properties of the films remain similar. This fact is due to the similar magnetic properties of the Fe_5Si_3 and Fe_3Si phases. The saturation magnetization of the latter one is higher than the one of Fe_5Si_3, but the overall magnetization of the films is the same due to the lower concentration of the Fe_3Si phase as was shown with EXAFS. The saturation magnetization of the SiC_xN_y:Fe films is close to the one of the materials based on ZnO and $A^{III}B^V$ compounds, making SiC_xN_y:Fe films an interesting and promising material for further study.

The material conductivity is another important parameter for the creation of a ferromagnetic semiconductor. Detailed analysis of the undoped SiC_xN_y film conductivity was carried out by different authors.[51,52] Summarizing these data, the following tendencies can be outlined:

1. With the deposition temperature rising the SiC_xN_y film conductivity tends to grow due to the variable range hopping mechanism which comes into action with the formation of crystals of SiC and Si_3N_4.

Fig. 8 (a) Magnetization curves of the SiC_xN_y:Fe films deposited at 900–1000 °C from a He-containing gas mixture, and (b) magnetization curves in the −250–250 Oe magnetic field range.

This journal is © The Royal Society of Chemistry 2019

J. Mater. Chem. C, 2019, **7**, 4250–4258 | **4255**

2. Carbon concentration growth leads to the formation of a free carbon phase, which exists as an amorphous one or as a graphite crystal. The latter ones possess larger conductivity compared to the amorphous matrix.

3. Nitrogen concentration growth results in the formation of a highly defective carbon phase with a structure similar to the amorphous one. Thus, the conductivity of SiC_xN_y films lowers with the N concentration rising.

Obviously, the Fe-doping of SiC_xN_y films may change the charge transfer mechanism. The electrical conductivity of SiC_xN_y:Fe films *vs.* deposition temperature for different gaseous mixtures is summarized in Table 1.

The following statements describe the observed tendencies:

1. The conductivity of SiC_xN_y films doped with Fe is higher than the one of the undoped films. The formation of iron-containing species gives rise to new charge transfer mechanisms, such as variable range hopping, typical for systems of an insulator matrix with embedded metal clusters.

2. SiC_xN_y:Fe films deposited at 1000 °C possess the highest conductivity among all of the samples due to the high iron concentration up to 10 at% and formation of iron silicide crystal phases such as Fe_5Si_3 and FeSi, which have higher conductivity than amorphous SiC_xN_y.

3. Substitution of helium for hydrogen or ammonia results in the conductivity decreasing. The composition of the amorphous matrix changes significantly from the one enriched with carbon, to the one close to SiN_x.

The conductivity of SiC_xN_y:Fe films may be changed in a very wide range from 10^{-12} to 6.9×10^{-4} S cm^{-1}. However, the films deposited below 900 °C are paramagnetic and have no prospective application for spintronics. For the ferromagnetic films deposited in the temperature range of 900–1000 °C the conductivity can be tuned 1.6×10^{-7}–6.9×10^{-4} S cm^{-1}, which represents more than 3 orders of magnitude. Moreover, the conductivity of the films deposited at 1000 °C may vary from 2.0×10^{-5} to 6.9×10^{-4} S cm^{-1}, while their saturation magnetization and coercivity remain constant. These films have the highest saturation magnetization among all of the obtained SiC_xN_y:Fe films. This fact combined with the conductivity being similar to the one of Si makes this material a promising candidate for the creation of spin injectors into silicon. The substitution of helium for hydrogen or ammonia results in a lower conductivity of the films, which may be useful for creation of spin-polarized current detectors. One can conclude that it is possible to tailor the transport properties of the material through the variation of the amorphous matrix composition without any change of its magnetic properties. This fact can be considered as a significant advantage when SiC_xN_y:Fe films are compared to other ferromagnetic semiconductors. The saturation magnetization and Curie temperature of d-metal doped ZnO are lower than the ones of SiC_xN_y:Fe films.[7–9] Applications of ferromagnetic materials based on $(Bi,Sb)_2Te_3$ with tunable conductivity are limited due to the low Curie temperature.[18] The promising ferromagnetic semiconductor $Co_{28.6}Fe_{12.4}Ta_{4.3}B_{8.7}O_{46}$ with variable conductivity and properties exceeding other materials[12] was obtained in a bulk form, while thin film materials are required for spintronics applications.

Unfortunately, the mechanism of charge transfer in SiC_xN_y:Fe films is studied insufficiently and remains an important question for future research. In similar systems of dielectric matrixes, *e.g.* Ca–F and Al–O, with inclusions of metal particles the mechanism of electron transport is often represented as variable range hopping (VRH) between metallic particles. One can assume that the conductivity of the SiC_xN_y:Fe films follows a similar pattern. Still, this assumption is to be confirmed for better understanding and more precise control of the functional properties of SiC_xN_y:Fe films.

Conclusions

Ferromagnetic films SiC_xN_y:Fe with variable composition were synthesized using the CVD technique. Thorough structural analysis revealed the composite nature of the material: Fe_3Si, Fe_5Si_3, SiC, and graphite crystals are embedded into the amorphous SiC_xN_y matrix. Variation of the deposition temperature allowed us to change the iron concentration from 0 to 10 at%. As a consequence, we can control the saturation magnetization of the film, making it as high as 20 emu cm^{-3}. The saturation magnetization of the SiC_xN_y:Fe films may be improved through the elevation of the iron concentration. The approach should be studied carefully due to the possible influence of higher ferrocene concentrations on the phase composition. Currently, the low coercivity of 20 Oe related to the presence of iron silicides indicates that the films are soft-magnetic. The analysis of the magnetic properties of the SiC_xN_y:Fe films revealed that the films deposited at 1000 °C possess the highest saturation magnetization, which can be useful for further spin-polarized charge-transfer research and application in the spintronics field. The interconversion of iron silicides discovered by EXAFS analysis may provide an effective tool to control the magnetic properties in a very precise way, but this promising direction of this work is yet to be studied. Variation of the gas phase composition is a useful tool to control the SiC_xN_y matrix composition. With the substitution of helium for hydrogen and ammonia the conductivity of the films changes from 6.9×10^{-4} to 10^{-12} S cm^{-1}. The conductivity of the ferromagnetic films can be changed by 3 orders of magnitude, providing an opportunity to tailor the properties in a wide range. It should be noted that while the conductivity of the films changes, the saturation magnetization and coercivity remain constant. The magnetic characteristics of the films deposited at 1000 °C combined with the conductivity close to the one of Si make these films promising materials for further analysis of spin-polarized charge transfer. The study of spin injection processes from SiC_xN_y:Fe films to Si may provide insights useful for the spintronics field and reveal tendencies which will shed some light on the transfer mechanism in amorphous semiconductors.

Conflicts of interest

There are no conflicts to declare.

Acknowledgements

Notes and references

1 V. Sverdlov and S. Selberherr, *Phys. Rep.*, 2015, **585**, 1–40.

2 G. A. Prinz, *Phys. Today*, 1995, **48**, 58–63.

3 T. Nie, in *Reference Module in Materials Science and Materials Engineering*, Elsevier, 2016, pp. 1–5.

4 D. D. Awschalom and M. E. Flatté, *Nat. Phys.*, 2007, **3**, 153–159.

5 S. I. Andronenko and S. K. Misra, *Appl. Magn. Reson.*, 2015, **46**, 693–707.

6 M. Bououdina, Y. Song and S. Azzaza, *Nano-Structured Diluted Magnetic Semiconductors*, Elsevier Ltd., 2016.

7 Y. Köseoğlu, *Ceram. Int.*, 2015, **41**, 11655–11661.

8 D. Saikia and J. P. Borah, *J. Mater. Sci.: Mater. Electron.*, 2017, **28**, 8029–8037.

9 Q. Mahmood, M. Hassan and M. A. Faridi, *Chin. Phys. B*, 2017, **26**, 027503.

10 A. Fert, *Angew. Chem., Int. Ed.*, 2008, **47**, 5956–5967.

11 Y. Yang, Z. Wu, W. Yang, J. Li, S. Chen and C. Li, *Appl. Phys. Express*, 2017, **10**, 063001.

12 W. Liu, H. Zhang, J. A. Shi, Z. Wang, C. Song, X. Wang, S. Lu, X. Zhou, L. Gu, D. V. Louzguine-Luzgin, M. Chen, K. Yao and N. Chen, *Nat. Commun.*, 2016, **7**, 13497.

13 N. Kobayashi, H. Masumoto, S. Takahashi and S. Maekawa, *Nat. Commun.*, 2014, **5**, 4417.

14 T. N. Koltunowicz, P. Zukowski, V. Bondariev, J. A. Fedotova and A. K. Fedotov, *Vacuum*, 2015, **120**, 44–50.

15 N. I. Fainer, M. L. Kosinova, Y. M. Rumyantsev, E. A. Maximovskii and F. A. Kuznetsov, *J. Phys. Chem. Solids*, 2008, **69**, 661–668.

16 N. I. Fainer, M. L. Kosinova, Y. M. Rumyantsev, E. A. Maksimovskii, F. A. Kuznetsov, V. G. Kesler, V. V. Kirienko, B. S. Han and C. Lu, *Glass Phys. Chem.*, 2005, **31**, 427–432.

17 E. Arias-egido, M. A. Laguna-marco, C. Piquer, R. Boada and S. Díaz-Moreno, *Adv. Funct. Mater.*, 2019, **29**, 1806754.

18 Y. Ou, C. Liu, L. Zhang, Y. Feng, G. Jiang, D. Zhao, Y. Zang, Q. Zhang, L. Gu, Y. Wang, K. He, X. Ma and Q. Xue, *APL Mater.*, 2016, **4**, 086101.

19 S. Omar and B. J. van Wees, *Phys. Rev. B*, 2017, **95**, 081404.

20 A. Bouravleuv, V. Sapega, V. Nevedomskii, A. Khrebtov, Y. Samsonenko, G. Cirlin and V. Strocov, *J. Cryst. Growth*, 2017, **468**, 680–682.

21 M. Zhong, M. Zhu, Z. Zhang, M. Zhong, M. Tariq, Y. Li, W. Li, H. Jin, K. Skotnicova and Y. Li, *Ceram. Int.*, 2016, **43**, 3166–3170.

22 A. K. Rana, Y. Kumar, P. Rajput, S. N. Jha, D. Bhattacharyya and P. M. Shirage, *ACS Appl. Mater. Interfaces*, 2017, **9**, 7691–7700.

23 E. Ermakova, Y. Rumyantsev, A. Shugurov, A. Panin and M. Kosinova, *Appl. Surf. Sci.*, 2015, **339**, 102–108.

24 E. Tomasella, F. Rebib, M. Dubois, J. Cellier and M. Jacquet, *J. Phys.: Conf. Ser.*, 2008, **100**, 082045.

25 S. Chikazumi, *J. Appl. Phys.*, 1961, **32**, S81.

26 Y. Wang, T. Jiang, L. Zhang and L. An, *J. Am. Ceram. Soc.*, 2009, **92**, 1603–1606.

27 P. Hoffmann, O. Baake, B. Beckhoff, W. Ensinger, N. Fainer, A. Klein, M. Kosinova, B. Pollakowski, V. Trunova, G. Ulm and J. Weser, *Nucl. Instrum. Methods Phys. Res., Sect. A*, 2007, **575**, 78–84.

28 P. S. Hoffmann, N. I. Fainer, O. Baake, M. L. Kosinova, Y. M. Rumyantsev, V. A. Trunova, A. Klein, B. Pollakowski, B. Beckhoff and W. Ensinger, *Thin Solid Films*, 2012, **520**, 5906–5913.

29 B. Doucey, M. Cuniot, R. Moudni, F. Ténégal, J. E. Bourée, D. Imhoff, M. Rommeluére and J. Dixmier, *J. Mater. Sci.*, 2002, **37**, 2737–2745.

30 A. M. Wrobel, I. Blaszczyk-Lezak, P. Uznanski and B. Glebocki, *Plasma Processes Polym.*, 2011, **8**, 542–556.

31 A. M. Wrobel, I. Blaszczyk-Lezak, P. Uznanski and B. Glebocki, *Chem. Vap. Deposition*, 2010, **16**, 211–215.

32 N. I. Fainer, A. G. Plekhanov, A. N. Golubenko, Y. M. Rumyantsev, V. I. Rakhlin, E. A. Maximovski and V. R. Shayapov, *ECS J. Solid State Sci. Technol.*, 2014, **4**, N3153–N3163.

33 A. C. Ferrari, *Solid State Commun.*, 2007, **143**, 47–57.

34 R. V. Pushkarev, N. I. Fainer and K. K. Maurya, *Superlattices Microstruct.*, 2017, **102**, 119–126.

35 Q. G. Fu, H. J. Li, X. H. Shi, K. Z. Li, J. Wei and Z. B. Hu, *Mater. Chem. Phys.*, 2006, **100**, 108–111.

36 S. M. Manakov and T. I. Taurbayev, *J. Nanoelectron. Opto-electron.*, 2012, **7**, 619–622.

37 C. J. Oliphant, C. J. Arendse, G. F. Malgas, D. E. Motaung, T. F. G. Muller, S. Halindintwali, B. A. Julies and D. Knoesen, *J. Mater. Sci.*, 2009, **44**, 2610–2616.

38 P. Mahanandia, P. N. Viswakarma, P. V. Bhotla, S. V. Subramanyam and K. K. Nanda, *Bull. Mater. Sci.*, 2010, **33**, 215–220.

39 V. Prasad and S. V. Subramanyam, *Phys. B*, 2005, **369**, 168–176.

40 A. Dasgupta, P. A. Premkumar, F. Lawrence, L. Houben, P. Kuppusami, M. Luysberg, K. S. Nagaraja and V. S. Raghunathan, *Surf. Coat. Technol.*, 2006, **201**, 1401–1408.

41 H. Cao, G. Huang, S. Xuan, Q. Wu, F. Gu and C. Li, *J. Alloys Compd.*, 2008, **448**, 272–276.

42 N. I. Fainer, A. N. Golubenko, Y. M. Rumyantsev, V. G. Kesler, E. A. Maximovskii, B. M. Ayupov and F. A. Kuznetsov, *Glass Phys. Chem.*, 2013, **39**, 77–88.

43 J. Lacaze and B. Sundman, *Metall. Trans. A*, 1991, **22**, 2211–2223.

44 A. L. Schmitt, J. M. Higgins, J. R. Szczech and S. Jin, *J. Mater. Chem.*, 2010, **20**, 223–235.

45 T. Nakayamada, K. Matsuo, Y. Hayashi, A. Izumi and Y. Kadotani, *Thin Solid Films*, 2008, **516**, 656–658.

46 T. Shinjo, Y. Nakamura and N. Shikazono, *J. Phys. Soc. Jpn.*, 1963, **18**, 797–801.

This journal is © The Royal Society of Chemistry 2019

J. Mater. Chem. C, 2019, **7**, 4250–4258 | 4257

47 M. K. Kolel-Veetil and T. M. Keller, *Materials*, 2010, **3**, 1049–1088.

48 M. Strečková, J. Füzer, L. Kobera, J. Brus, M. Fáberová, R. Bureš, P. Kollár, M. Lauda, Ĺ. Medvecký, V. Girman, H. Hadraba, M. Bat'Ková and I. Bat'Ko, *Mater. Chem. Phys.*, 2014, **147**, 649–660.

49 S. W. Hung, T. T. J. Wang, L. W. Chu and L. J. Chen, *J. Phys. Chem. C*, 2011, **115**, 15592–15597.

50 Y. Jing, J. Liu, W. Ji, W. Wang, S. He, X. Jiang, T. Wiedmann, C. Wang and J. Wang, *ACS Appl. Mater. Interfaces*, 2015, **7**, 12649–12654.

51 N. I. Fainer, M. L. Kosinova, Y. M. Rumyantsev, E. A. Maximovskii and F. A. Kuznetsov, *J. Phys. Chem. Solids*, 2008, **69**, 661–668.

52 B. Ma, Y. Wang, K. Wang, X. Li, J. Liu and L. An, *Acta Mater.*, 2015, **89**, 215–224.

This journal is © The Royal Society of Chemistry 2019